RSC Advances

PAPER

View Article Online
View Journal | View Issue

Cite this: *RSC Adv.*, 2025, **15**, 16469

Investigation of shielding properties of $Se_{100-y}(AgX)_y$ ($y = 0$, 5 and X = Cl, Br, and I) glass-ceramics

Anil Kumar, Shiv Kumar Pal and Neeraj Mehta *

The $Se_{100-y}(AgX)_y$ ($y = 0$, 5 and X = Cl, Br, and I) glass-ceramics were synthesised *via* melt-quenching, with density measured using Archimedes' principle. Radiation-shielding properties were investigated using *Phy-X/PSD* across a range of 15 keV to 15 MeV, assessing parameters such as LAC, MAC, MFP, Z_{eff}, N_{eff}, C_{eff}, $Z_{eq.}$, EABF, EBF, and FNRCS. The $Se_{95}(AgBr)_5$ sample exhibited the lowest HVL, indicating superior photon attenuation compared to other compositions. The attenuation percentage (RPE%) was investigated experimentally across 60 keV, 81 keV, and 100 keV measured using Scanditronix stereotactic field diode (SFD) detectors. Additionally, their shielding performance was compared with commercially used materials, including ordinary concrete and radiation-shielding glasses. Results demonstrate that $Se_{95}(AgBr)_5$ meets key shielding criteria, making it a promising alternative for low-energy radiation protection. Incorporating silver halides significantly influences shielding efficiency, with AgBr proving the most effective. These findings highlight the potential of AgBr-doped selenium glass-ceramics as efficient radiation-shielding materials, offering a viable replacement for traditional options in specific shielding applications.

Received 5th February 2025
Accepted 28th April 2025

DOI: 10.1039/d5ra00865d

rsc.li/rsc-advances

1. Introduction

As technology advances, individuals are increasingly exposed to ionizing electromagnetic radiation from various sources, including background radioactivity, milling, nuclear power plants, mining that uses synthetic radioactive isotopes, nuclear research, space exploration, and other sectors. It's crucial to acknowledge that radiation exposure can result in a range of health problems, from carcinomas to genetic disorders and tissue damage. Moreover, ionizing radiation can modify the physical and chemical characteristics of soil, rock, and water, adversely affecting biodiversity and ecosystems. Therefore, conducting thorough investigations and adopting adequate protection and shielding measures are essential, as these hazards present substantial risks to human health.[1–3] Protection can be achieved through efficient shielding, which requires comprehensive research into potential shielding materials, considering their mechanical properties, radiation attenuation characteristics, anticipated energy levels, costs, availability, manufacturability, performance, and affordability.[4] A critical attribute of shielding materials is their resistance to potential damage caused by exposure to electromagnetic radiation, ensuring they are non-toxic. In addition to having a high radiation absorption cross-section, an effective shielding material must also provide significant attenuation of incoming radiation over a minimal penetration depth. Depending on the specific application requirements, different materials are employed for this purpose. For instance, ordinary concrete is commonly used to absorb X-rays in the exterior walls of X-ray rooms due to its effectiveness in radiation attenuation. While concrete is ideal for certain applications, alternative materials are also utilized. Glasses enhanced with metallic additives can function as radiation-shielding materials. Adding heavy metal additives increases the density of the glass, thereby improving its shielding properties. Techniques such as melt quenching can be used to create these glass ceramics. Given their cost-effectiveness and ease of production, glasses are often considered alternative materials for radiation shielding. Silver halide-incorporated glassy materials have been explored for various optical applications due to their excellent infrared transmission properties.[5–9] However, their potential for radiation shielding is less well-known but of growing interest due to the presence of heavy elements like silver (Ag), which can contribute to radiation attenuation.[10–12] Silver halide glass ceramics containing silver (Ag) have a high atomic number, which is crucial for effective radiation shielding. The high atomic number enhances the photoelectric effect, leading to better absorption of X-rays and gamma rays. This makes these materials potentially useful in environments where radiation protection is required.[13,14] The effect of silver iodide (AgI) content addition on the physicochemical characteristics such as molar volume, excess volume, packing density, the average number of co-ordination, cross-linking density, number of constraints,

---

Department of Physics, Institute of Science, Banaras Hindu University, Varanasi 221005, India. E-mail: dr_neeraj_mehta@yahoo.co.in

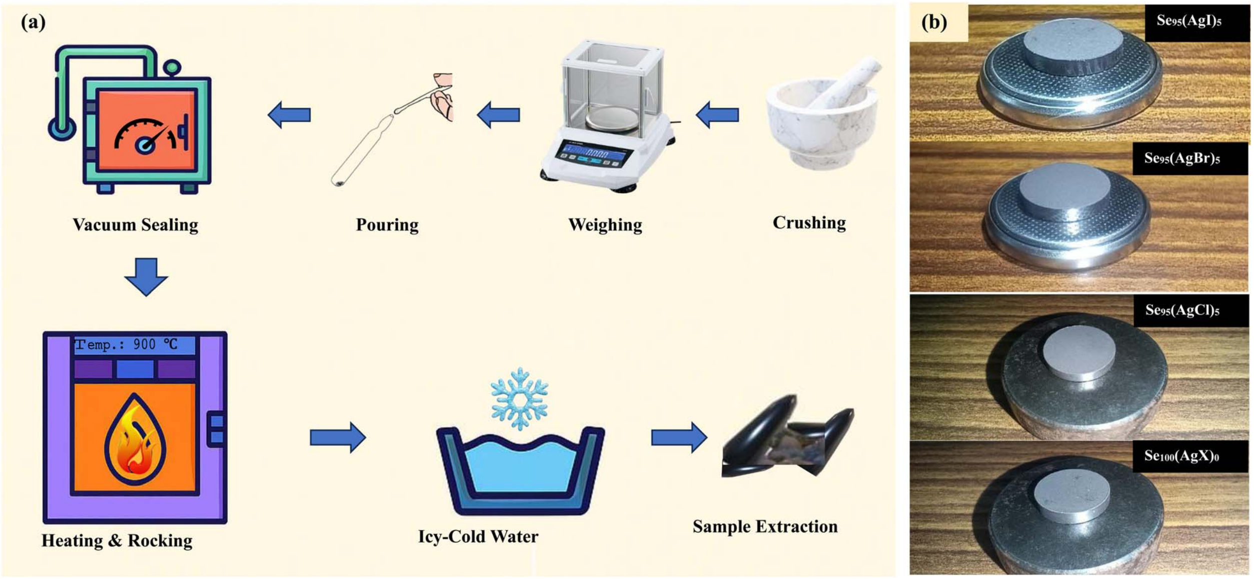

Fig. 1 (a) Synthesis process (b) polished pellet of $Se_{95}(AgBr)_5$ sample.

mean bond energy and compactness of chalcohalide glassy $(0.5As_2Se_3{-}0.5GeTe)_{100-x}(AgI)_x$ system has been studied by Kebaili *et al.*[5] Salimgareev *et al.*[6] investigated the effect of geometrical parameters of fibers based on silver halide fibers on the performance of a fiber-optic temperature control system at the temperatures of 295–395 K. They observed that a reduction in the fiber length leads to a linear increase in transmission values. The glassy series $(GeTe_{4.3})_{100-x}(AgI)_x$ ($x = 5, 10, 15, 20,$

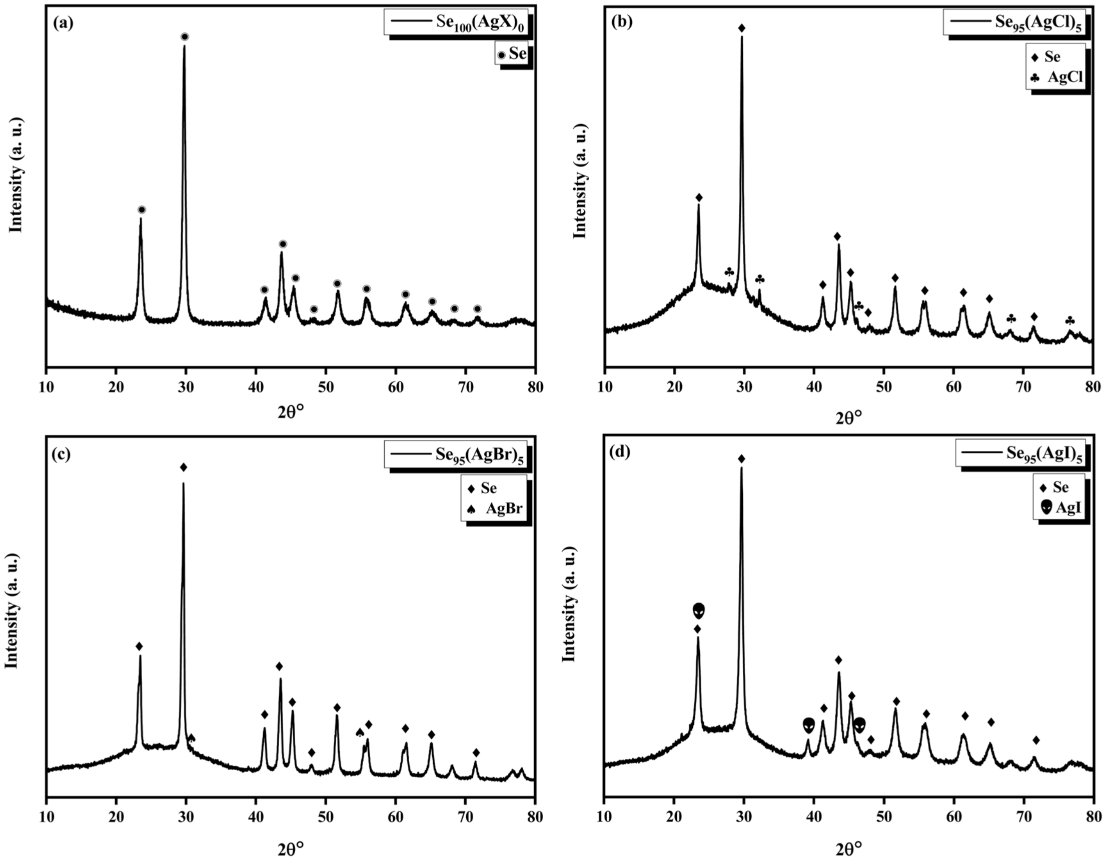

Fig. 2 XRD patterns of the present samples (a) $Se_{100}(AgX)_0$, (b) $Se_{95}(AgCl)_5$, (c) $Se_{95}(AgBr)_5$ and (d) $Se_{95}(AgI)_5$.

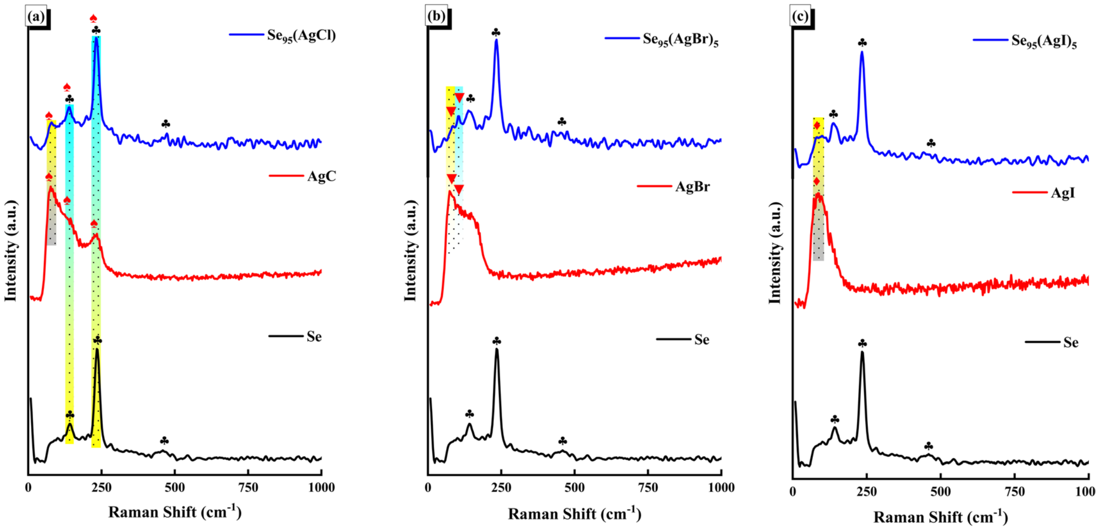

Fig. 3 Raman spectra of (a) AgCl, (b) AgBr and (c) AgI-incorporated Se samples at room temperature taken with 532 nm excitation laser.

25, 30 mol%) of chalcohalide glasses have been synthesized by Ding *et al.*[7] to study their potential in acousto-optic properties like refractive index, elastic modulus, density, acoustic velocity and attenuation. The structural and optical properties of europium-doped bismuth borate glasses by exposure to gamma radiation have been studied, and these results have been compared with virgin samples by Patwari *et al.*.[8]

In the literature, different properties of halogen-containing polymers and nanocomposites have been studied by different research communities.[15–19] However, there are various articles published based on chalcohalide glasses to study the different properties, but, no records were found for the study of radiation shielding characteristics of silver halide-containing

Table 1 Chemical compositions and abbreviated names, along with their densities, of the various chalcohalide glassy compositions

Chemical compositions (mol.%)					
Se	AgCl	AgBr	AgI	Density ($g\ cm^{-3}$)	Code name
100	0	0	0	4.18	$Se_{100}(AgX)_0$
95	5	0	0	4.48	$Se_{95}(AgCl)_5$
95	0	5	0	4.49	$Se_{95}(AgBr)_5$
95	0	0	5	4.21	$Se_{95}(AgI)_5$

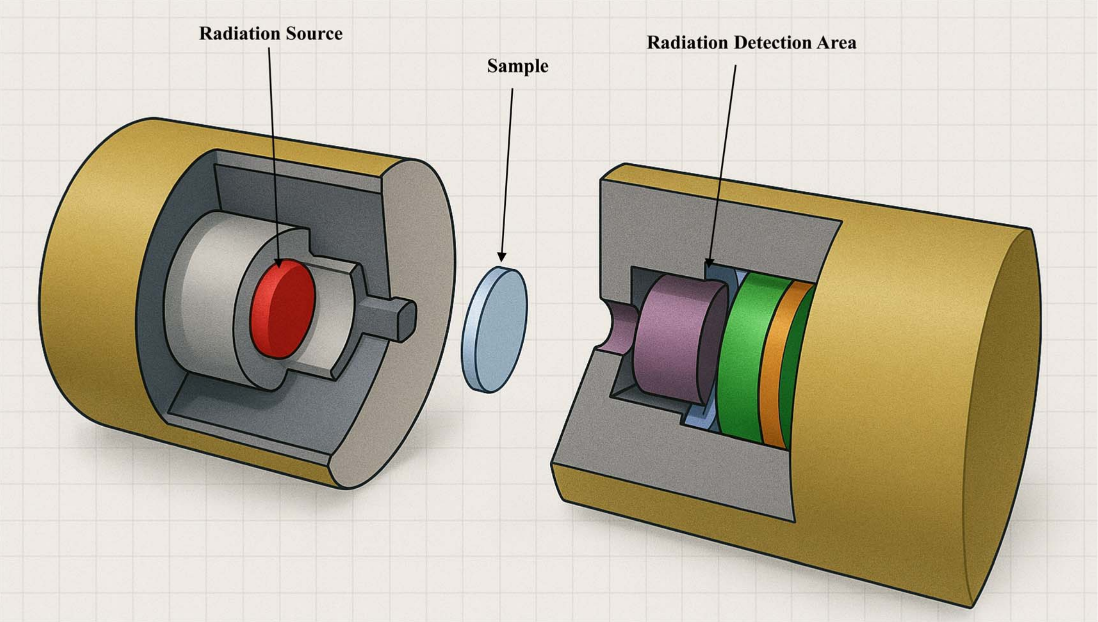

Fig. 4 Visual representation of simulation geometry.

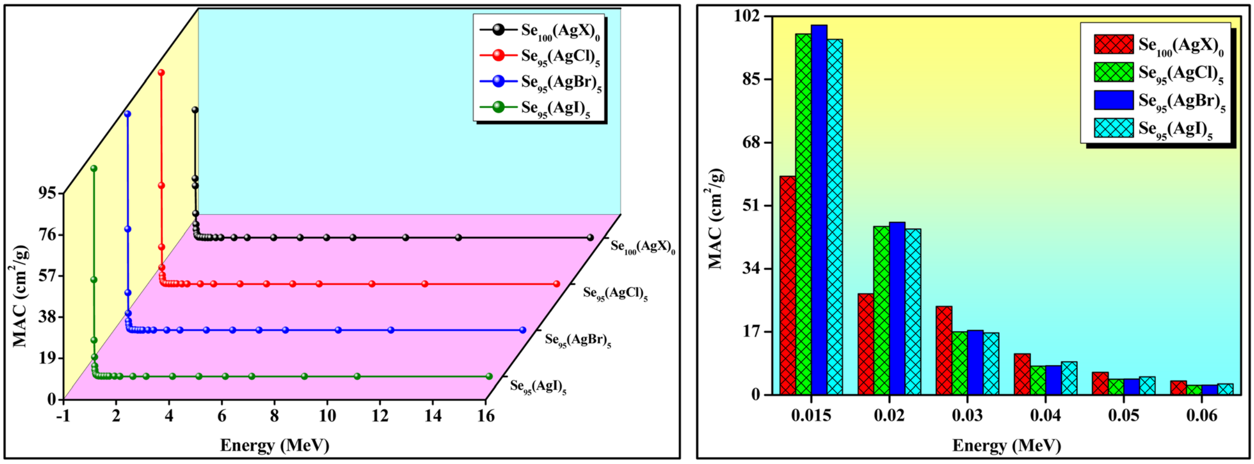

Fig. 5 Dependency of mass attenuation coefficient (MAC) on photon energy for Se and chalcohalide glass ceramics series.

chalcogenide glassy materials.[20–30] The presence of silver, combined with halides like bromine or iodine, contributes to the glass's ability to shield against ionizing radiation. The radiation-shielding competence of silver halide glasses can be further enhanced by modifying their composition. By varying halide elements, the density and atomic structure of the glass can be optimized to improve its attenuation properties while maintaining desirable optical characteristics. Utilizing their unique properties, silver halide chalcogenide glass-ceramics can be beneficial in specialized applications, such as nuclear medicine, radiation-shielding windows in nuclear facilities, and aerospace environments where both transparency in specific wavelengths and radiation protection are crucial.

Halogen elements combined with chalcogens represent an interesting class of materials with combined optical and radiation-shielding properties.[20–30] The addition of halide to chalcogenides significantly improves their ability to attenuate ionizing radiation, such as gamma rays and X-rays.[20–30] Selenium (Se) has a higher atomic number compared to other elements commonly found in glasses, contributing to the photoelectric absorption process, which is crucial for effective radiation shielding. Silver, being a heavy metal with a high atomic number, already provides substantial radiation shielding. When combined with selenium, the material benefits from a synergistic effect where both elements contribute to enhanced radiation absorption.[30] This combination increases the overall effectiveness of the glassy material in protecting against radiation. The density of the material plays a crucial role in its radiation-shielding properties. Incorporating metal halide into selenium typically increases the density, leading to a higher probability of interaction between the glass atoms and incoming radiation. This results in better attenuation of gamma rays and X-rays. The radiation-shielding properties of silver halides with selenium glasses can be optimized by adjusting the proportions of selenium and silver halides. Fine-tuning the glass composition makes it possible to achieve a balance between maximizing radiation-shielding effectiveness and maintaining other desirable properties, such as optical transparency and mechanical strength.

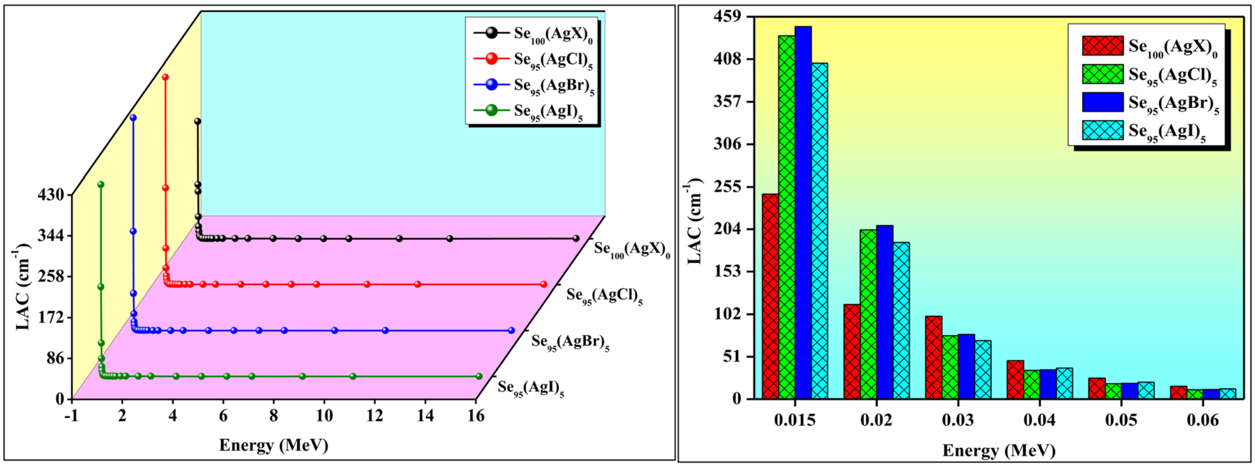

Fig. 6 Dependency of linear attenuation coefficient (LAC) on photon energy for all the samples.

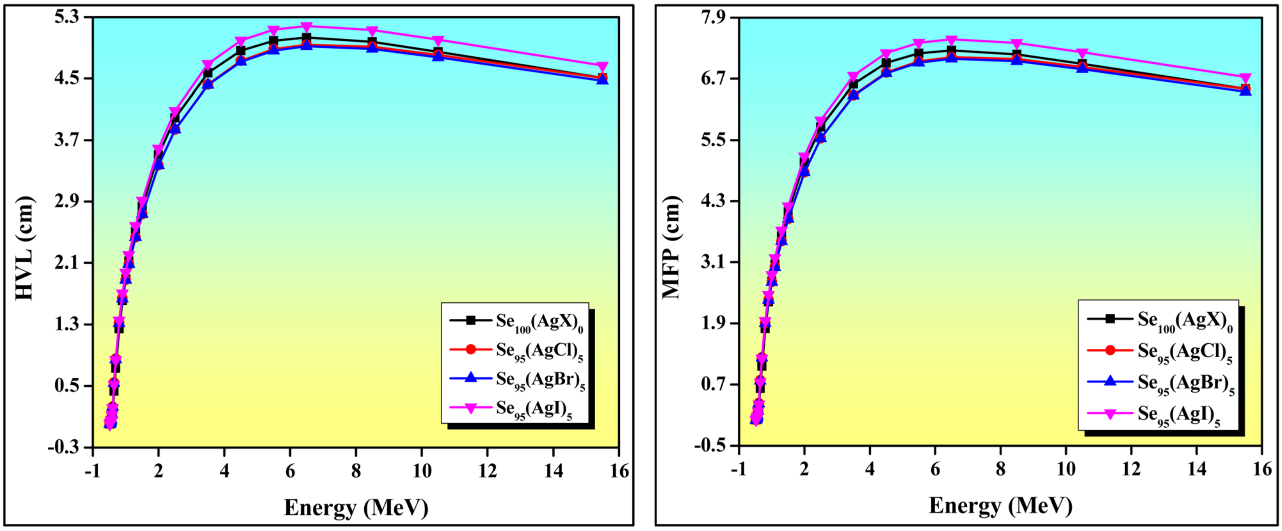

Fig. 7 Variation of half value layer (HVL) and mean free path (MFP) with photon energy for Se and chalcohalide glass ceramics series.

From the above literature survey, it is clear that several reports have been made on radiation shielding investigations possessing various types of materials. However, very few reports have been made on studying the radiation-shielding properties of chalcohalide glass ceramics. Therefore, this research paper aims to determine and optimize the radiation-shielding capability of silver halide-containing, selenium-based chalcogenide glass-ceramics to see the effect of different silver halide materials on selenium.

2. Materials and methods

The melt-quenching method was selected for its ability to produce homogeneous glass-ceramic samples with good control over composition and minimal crystallinity. This method is particularly effective for synthesizing chalcogenide and chalcohalide glass systems, allowing rapid cooling from high temperatures to retain the amorphous structure essential for our study. Furthermore, it facilitates the incorporation of silver halides uniformly within the selenium matrix, which is

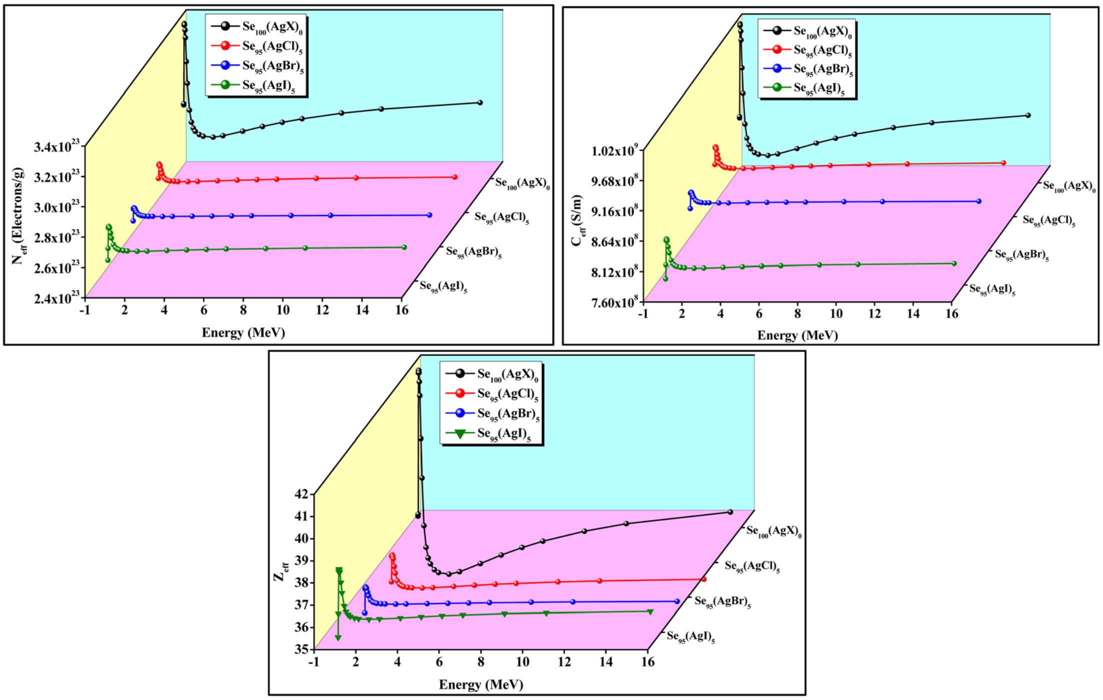

Fig. 8 Plots of the effective number of electrons (N_{eff}), effective conductivity (C_{eff}), and effective atomic number (Z_{eff}) with photon energy for all samples.

crucial for assessing their influence on radiation-shielding properties. To prepare the glassy samples under investigation, appropriate amounts of AgCl, AgBr, AgI, and Se, composed as $(Se)_{95}(AgX)_5$, where X represents Cl, Br, or I, were sealed within an evacuated quartz ampoule. This mixture was thoroughly combined in a rocking furnace at 800 °C for almost 10 hours. Subsequently, the melts were rapidly quenched in an ice-water mixture.[31,32] Fig. 1(a) Illustration of different steps involved in the melt-quench synthesis route. Fig. 1(b) shows images of the polished pellets from the freshly prepared samples. All four samples exhibit a similar appearance, primarily due to the high selenium content.

In our study, the density of each sample is a crucial parameter. We employed a straightforward and reliable method to determine the density of the four samples accurately. Using Archimedes' principle, the density of the synthesized samples was calculated. The weights of the bulk material in air (W_a) and liquid (W_l) were used in the following equation. When using water as the immersing liquid, the density of water (ρ_w) is taken as 1 g cm^{-3}.[1]

$$\rho = \frac{W_a}{W_a - W_l}\rho_l$$

3. Results and discussions

Phase analysis of these samples was performed by powder X-ray diffraction (XRD). Diffractograms were obtained using a PANalytical diffractometer (Cu Kα1, $\lambda = 1.54051$ Å). The scan range was 10–80° (2θ). The X-ray diffractograms of $Se_{95}(AgCl)_5$, $Se_{95}(AgBr)_5$ and $Se_{95}(AgI)_5$ samples are presented in Fig. 2(a–d). Few peaks of significant intensities were observed over the broad hump. The peaks are not very sharp, which shows the amorphous nature of the sample. XRD patterns indicate the presence of crystallinity, overlaying the amorphous glassy matrix. Trigonal selenium (t-Se) exhibits two strong and distinct diffraction peaks at $2\theta = 29.70°$ and 26.54°, attributed to the (100) and (101) lattice planes.[33] The peaks at 29.74° and 23.64° are correlated with the t-Se crystallographic planes present in all samples.[34] For the pure Se sample, Bragg reflections corresponding to the (100), (101), (110), $(10\bar{2})$, (111), (200), (201), (112), $(20\bar{2})$, (210), $(21\bar{1})$, and (113) sets of lattice planes are observed. They are well-matched with the JCPDS data (JCPDS file No. 96-901-2502).[35] For the $Se_{95}(AgCl)_5$ sample, the peaks were identified in the JCPDS profile. This profile confirms the presence of AgCl; Bragg reflections corresponding to the (111), (200), (220), (400) and (420) sets of lattice planes are observed and are well-matched with the JCPDS data (JCPDS file No. 96-901-1667). For the Se $Se_{95}(AgBr)_5$ sample, Bragg reflections corresponding to the (020) and (022) sets of lattice planes are observed and are well-matched with the JCPDS data (JCPDS file No. 96-901-1683), confirming the presence of AgBr cubic phases in the as-synthesized glassy-ceramic alloy. For the $Se_{95}(AgI)_5$ sample, Bragg reflections corresponding to the (111), (022) and (131) sets of lattice planes are observed and are well-matched with the JCPDS data (JCPDS file No. 96-901-1694).[36]

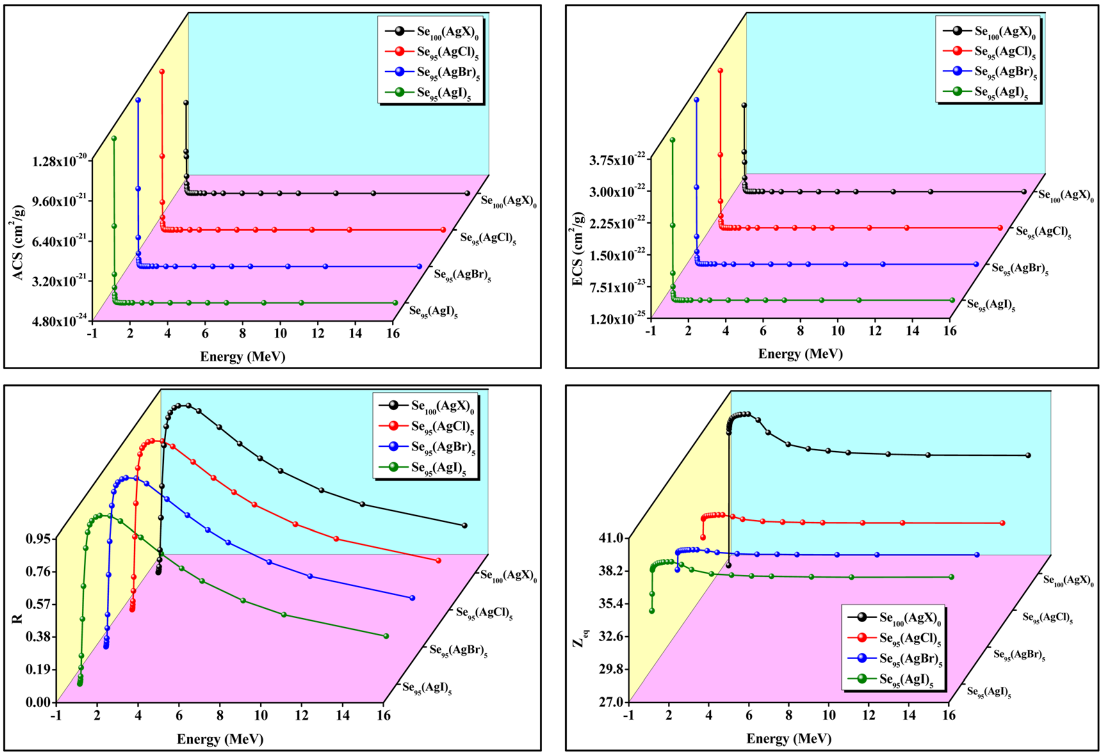

Fig. 9 Graphs between atomic cross-section (ACS), electronic cross-section (ECS), *R*, and equivalent atomic number ($Z_{eq.}$) against photon energy for Se and chalcohalide glass-ceramics.

Raman scattering spectra were acquired using a WITec alpha300R Raman spectrometer. Fig. 3 displays the Raman spectra obtained for the pure Se, AgCl, AgBr, AgI and $Se_{95}(AgCl)_5$, $Se_{95}(AgBr)_5$ and $Se_{95}(AgI)_5$ samples, all measured using a 532 nm excitation laser. The Raman peaks observed at 141.2 cm^{-1} and 459 cm^{-1} are attributed to the bending vibrations of Se–Se units arranged in a trigonal selenium-like (t-Se) conformation and the stretching vibrations of Se–Se bonds within Se_8 rings, respectively.[33,37] Additionally, the Raman band at 234 cm^{-1} is associated with the Se_n vibration mode of t-Se[38] caused by the vibration of the A_1 and E mode vibrations, as previously reported in the literature.[39]

The Raman spectra of AgCl and AgBr present a high fluorescence background characteristic of silver-based metallic materials.[40] The Raman peaks observed at 77 cm^{-1} and 231.5 cm^{-1} are attributed to the stretching mode of the Ag–Cl units.[41] As the AgCl amount is introduced into the Se, the fluorescence background is considerably reduced, and a characteristic Raman peak of AgCl begins to appear, located at approximately 79.6 cm^{-1}. Another characteristic Raman peak of AgCl is at 234.3 cm^{-1}, which merges with the Raman band of Selenium at 234 cm^{-1}. Doping with silver bromide or silver iodide does not significantly change the broad, poorly resolved spectral envelope of glassy Se. The Raman peaks observed at 74 cm^{-1} and 106 cm^{-1} are attributed to the stretching mode of the Ag–Br units. As the AgBr amount is introduced into the Se, the fluorescence background considerably reduces, and one characteristic Raman peak of AgBr begins to appear, located at approximately 82.6 cm^{-1}. Another characteristic Raman peak of AgBr is at exactly at 106 cm^{-1}. Peaks observed at 85 cm^{-1} are attributed to the stretching mode of the Ag–I units.[42] As the AgI amount is introduced into the Se, the characteristic Raman peak of AgBr begins to appear, located at approximately 82.6 cm^{-1}. Another characteristic Raman peak of AgBr is at exactly at 106 cm^{-1}.

The radiation shielding parameters of this synthesized series were simulated using a crucial open code software named *Phy-X/PSD* developed by Sakar *et al.*[43] in the energy range from 15 keV to 15 MeV. We employed the *Phy-X/PSD* software because of its reliability, accessibility, and wide acceptance in the

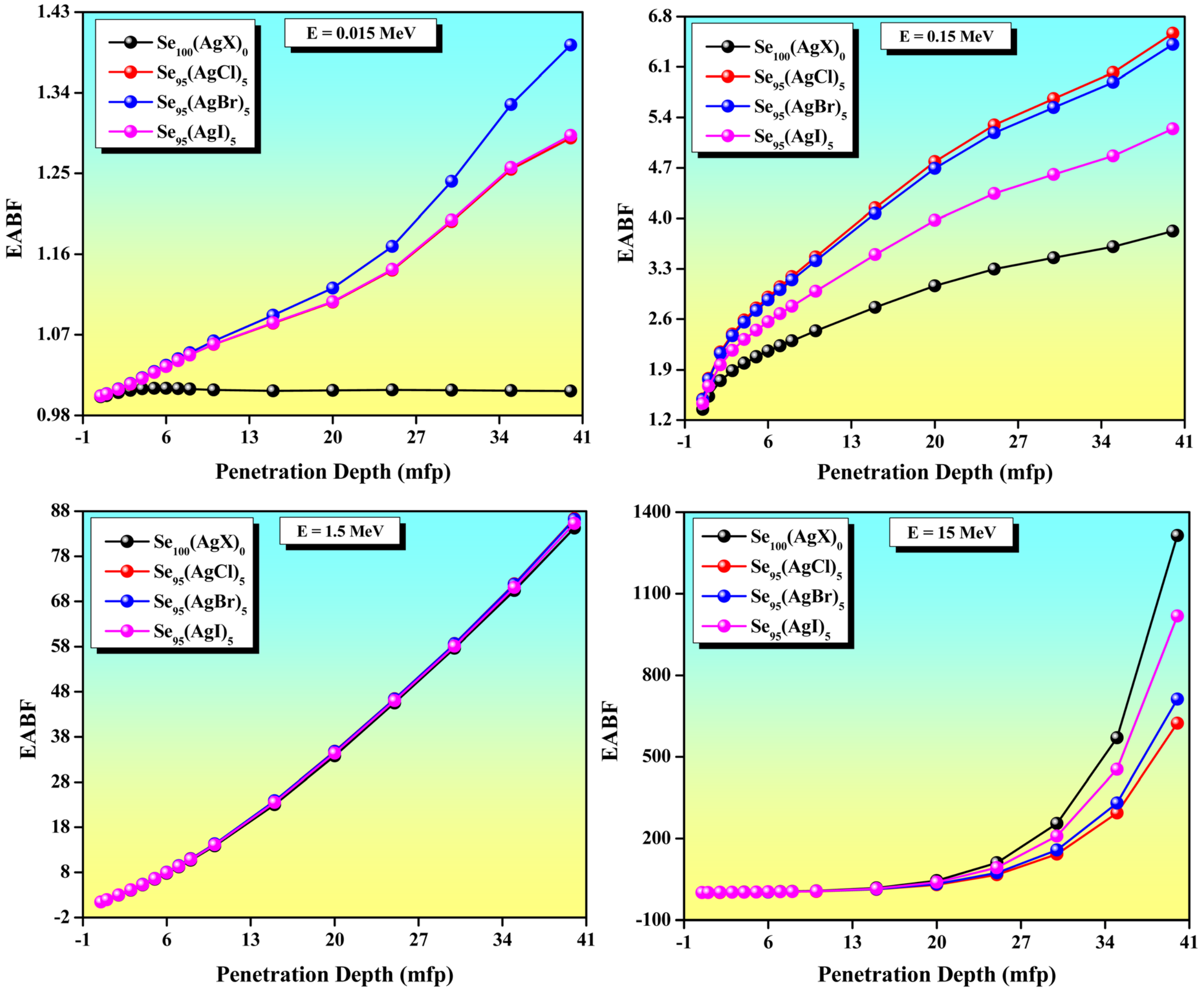

Fig. 10 Variation of energy absorption build-up factor (EABF) with penetration depth at four different values of photon energy for Se and chalcohalide glass-ceramics samples.

radiation-shielding research community. It allows comprehensive analysis over a broad energy spectrum (15 keV to 15 MeV). It calculates multiple shielding parameters (such as MAC, LAC, HVL, Z_{eff}, and buildup factors) that are critical for a thorough evaluation of radiation-shielding performance. This method relies on deterministic models based on elemental composition and density inputs. As these models are not derived from experimental repetitions but from computational simulations, statistical measures like mean ± standard deviation are not applicable. However, the experimental measurements (*e.g.*, density and RPE%) were conducted in triplicate, and average values are reported, with minimal variance observed.

Fig. 4 illustrates the visual representation of the simulation geometry. Table 1 lists the chemical compositions and densities of the synthesized samples. We used Archimedes' principle to determine the density of each sample.[44] One can see from Table 1 that the density of selenium is minimum, and the composition $Se_{95}(AgBr)_5$ has maximum density. The mass attenuation coefficient (MAC) varies with the photon energy, as shown in Fig. 5. In the low-energy region, the value of MAC decreases very rapidly with energy because photoelectric interaction plays a leading role. However, in the mid- and higher-energy regions, the variation of MAC is almost halted due to the domination of Compton and pair production interactions, as depicted in Fig. 5. The bar diagram shows that the maximum MAC value is observed in the $Se_{95}(AgBr)_5$ composition, while the minimum is noted in the Se sample within the low-energy region. These results show that the silver halides incorporated sample at low energies shows far better radiation shielding than the parent sample.

We observed a similar variation in LAC values with photon energy as seen with MAC, owing to the intrinsic interconnection between LAC and MAC. The extreme value of LAC was observed for the $Se_{95}(AgBr)_5$ composition compared to others in the low-energy region, as represented in the bar diagram of Fig. 6. Mahmoud *et al.*[45] suggested that the photoelectric interaction is dominated in the low-energy region because the cross-section of photoelectric interaction is proportional to $E^{-3.5}$. However, in the high-energy region, the observed dominant nature of the pair-production effect is due to the cross-section of pair production in the high-energy zone being proportional to the logarithm of the energy ($\log E$). The variation of HVL and MFP

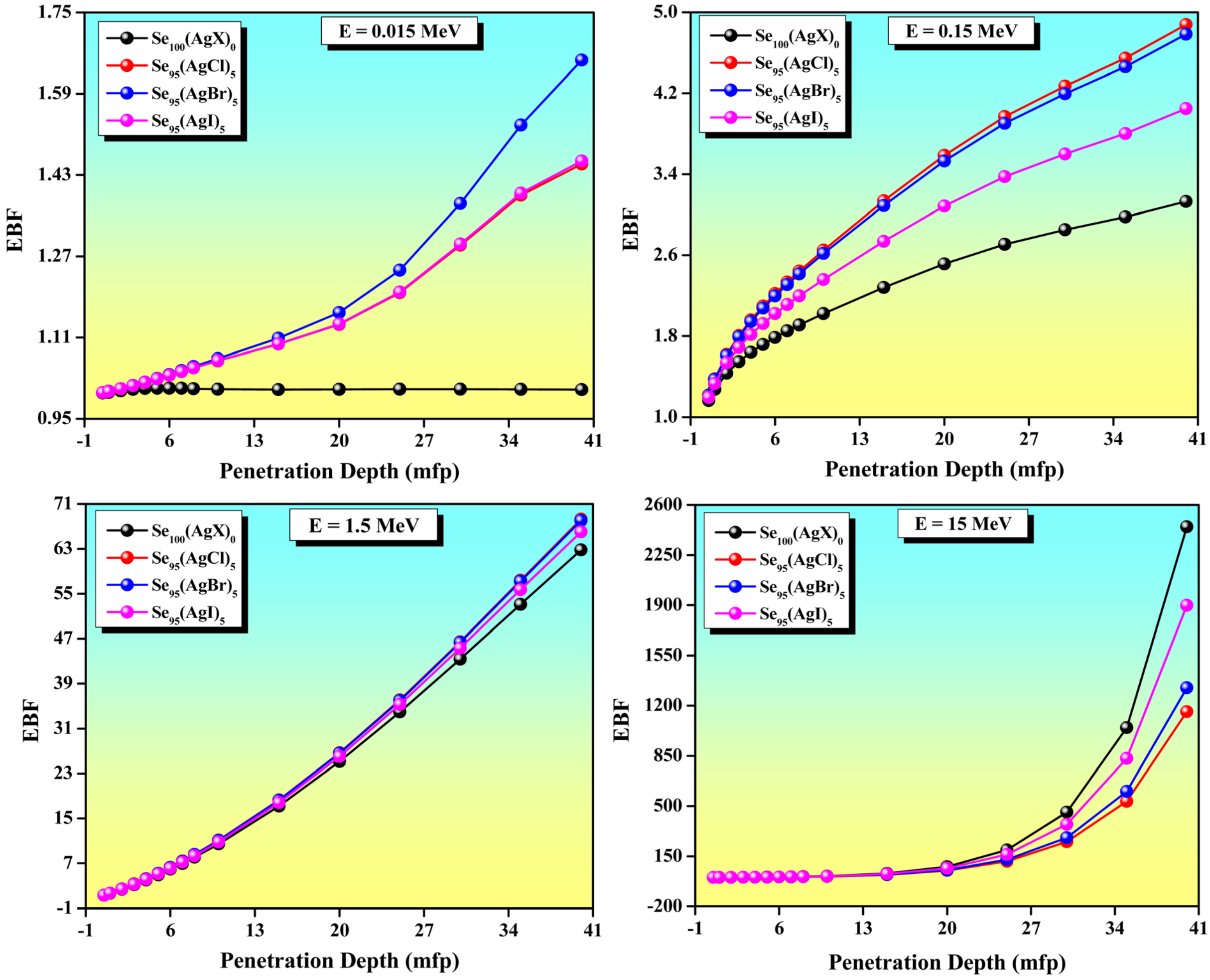

Fig. 11 Variation of exposure build-up factor (EBF) with penetration depth at four different values of photon energy for Se and chalcohalide glass-ceramics samples.

with energy is depicted in Fig. 7. Materials with low HVL and MFP values are considered better for radiation shielding. Based on the above-mentioned three interaction phenomena, the variation of HVL and MFP in the different energy regions can be understood.[45] Out of the current samples, $Se_{95}(AgBr)_5$ has a minimum value of HVL and MFP; however, $Se_{95}(AgI)_5$ has a maximum value, as shown in Fig. 7. When comparing these results with similar materials reported in the literature, we find that these results are significantly superior to others, such as ref. 1, 46 and 47. The effective atomic number (Z_{eff}) of photons refers to a value representing the combined atomic number of multiple elements, indicating how a composite material interacts with photons. Unlike the atomic number of individual elements, Z_{eff} is not a constant and varies depending on the material's composition.[48] Materials with a higher value of Z_{eff} have greater capabilities to attenuate gamma radiation because the probability of photoelectric absorption increases significantly at high values of Z_{eff}.[49] The dependencies of Z_{eff}, N_{eff}, and C_{eff} with photon energy are shown in Fig. 8, whose variations are very similar due to the mutual linear interconnection. The values of Z_{eff}, N_{eff}, and C_{eff} are significantly affected by incorporating different silver halides in the parent Se glass sample. A reduction in Z_{eff}, N_{eff}, and C_{eff} values was observed after adding silver halides; however, a very slight variation was noted among halide compositions. The extreme values of Z_{eff}, N_{eff}, and C_{eff} were observed at an energy of approximately 60 keV.

The variation of atomic cross-section (*ACS*), electronic cross-section (*ECS*), *R* (the ratio of Compton's partial mass attenuation coefficient to the total mass attenuation coefficient), and $Z_{eq.}$ with photon energy are illustrated in Fig. 9 for all investigated glass-ceramic compositions. ACS refers to the interaction probability per unit volume of material per atom, while ECS represents the interaction probability per unit volume of material per electron.[43,50] The maximum values of ACS and ECS were found for $Se_{95}(AgBr)_5$ composition at 15 keV radiation energy. The variation of ACS and ECS with photon energy can be understood in the photoelectric effect, Compton effect, and pair production interaction phenomena in low, mid, and high energy regions, respectively. Primarily, the value of *R* and $Z_{eq.}$ has been rising sharply with increasing energy and has decayed gradually in high-energy regions. The extreme value of *R* and $Z_{eq.}$ is observed for $Se_{95}(AgCl)_5$ and Se composition at 1.5 MeV energy, respectively, as illustrated in Fig. 9. The involvement of colliding photons in the material target is represented by the build-up factor parameter of radiation-shielding materials.[51] The geometrical progression (G–P) fitting parameters and value of $Z_{eq.}$[52,53] were utilized to find out the value of the energy absorption build-up factor (EABF) and exposure build-up factor (EBF). The Exposure Build-up Factor (EBF) quantifies the increase in radiation exposure due to scattered radiation in a shielding material. When photons (like gamma rays or X-rays) pass through a material. Some interact *via* photoelectric effect,

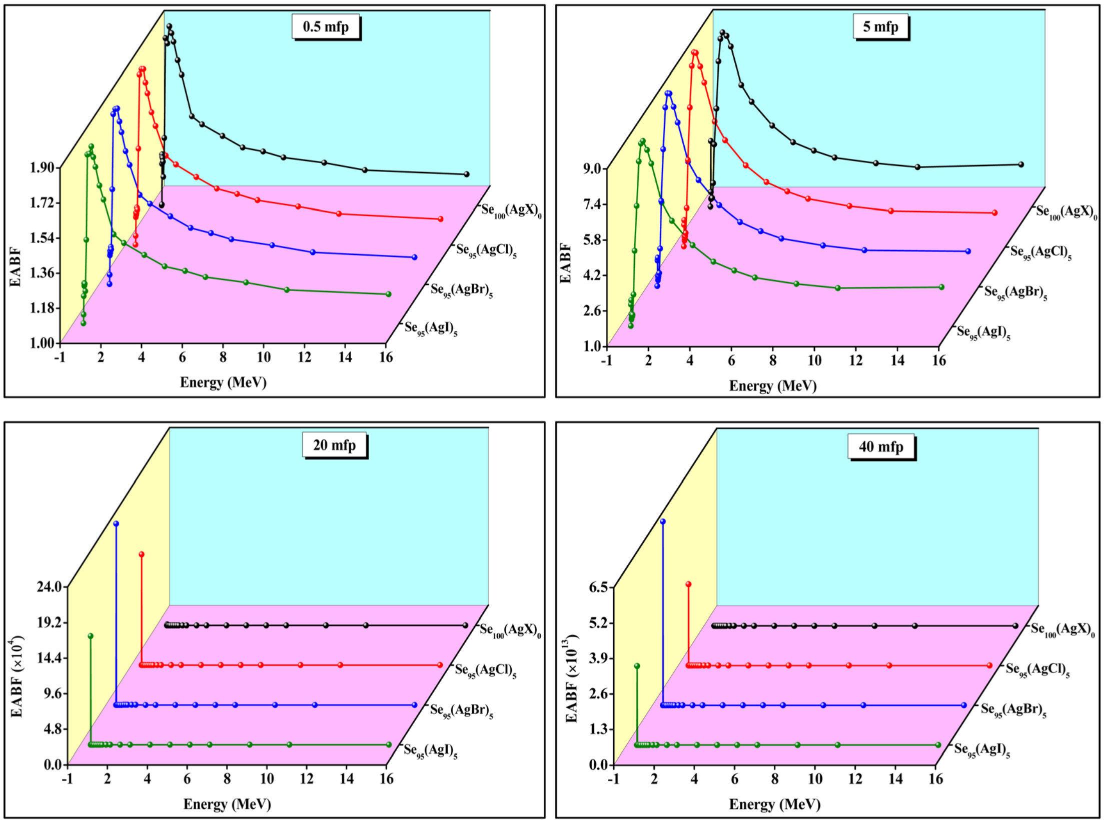

Fig. 12 Graphs between energy absorption build-up factor (EABF) *versus* photon energy at four different values of penetration depth for all materials in the current study.

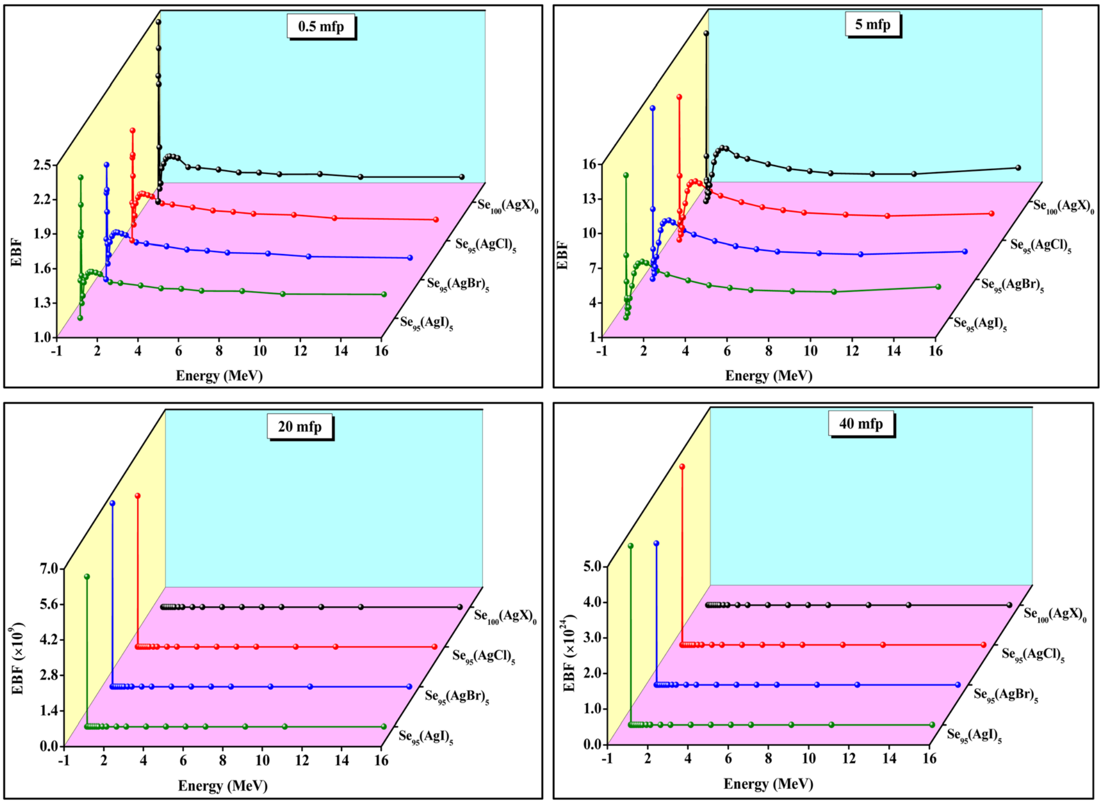

Fig. 13 Graphs between exposure build-up factor (EBF) *versus* photon energy at four different values of penetration depth for Se and chalcohalide glassy series.

Compton scattering, or pair production. Scattered photons may still reach the point of measurement. EBF accounts for this increase in dose due to those scattered photons.[54] The value of EABF and EBF as a function of penetration depth is illustrated in Fig. 10 and Fig. 11, respectively, at four different energy values. Both EABF and EBF increase linearly with the increase in the value of penetration depth in the low and mid-zone of energy, while at high energy (*i.e.*, 15 MeV), its variation is of an exponential type for the investigated sample series.

The variation of EABF and EBF with photon energy is shown in Fig. 12 and Fig. 13, respectively, for four different penetration depths (0.5, 5, 20, and 40 mfp). At the low value of penetration depth (*i.e.*, 0.5 and 5 mfp), we have observed some peaks in the lower energy zone that indicate the domination of the photoelectric effect in this region. This occurs when the photon energy matches the electron's binding energy in the K, L-I, and L-II shells.[55] In regions where particle build-up is restricted, gamma-ray absorption primarily occurs in the low and high-energy ranges. In contrast, Compton scattering is the predominant mechanism observed in the mid-energy zone, though it does not result in absolute photon loss.[52] The value of EABF is maximum for $Se_{95}(AgBr)_5$ composition at the high value of penetration depth (*i.e.*, 20 and 40 mfp) and minimum for the parent Se sample. However, the value of EBF is found to be maximum for $Se_{95}(AgBr)_5$ composition at the mid-value of penetration depth (*i.e.*, 5 and 20 mfp). The extreme value of the removal cross-section that indicates the attenuation of fast neutrons (FNRCS) is observed for $Se_{95}(AgCl)_5$ composition, as shown in the bar diagram of Fig. 14.[56,57]

Radiation Protection Efficacy (RPE) measures a material's effectiveness in attenuating or shielding radiation.[58,59] It quantifies how well a material reduces the intensity of incident radiation, directly indicating its performance as a radiation shield. Fig. 15(a) compares the theoretical RPE% of the

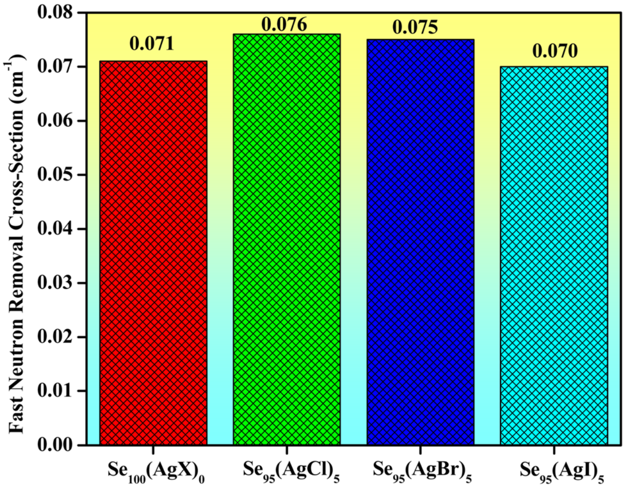

Fig. 14 Bar diagram of fast neutron removal cross-section for all the samples.

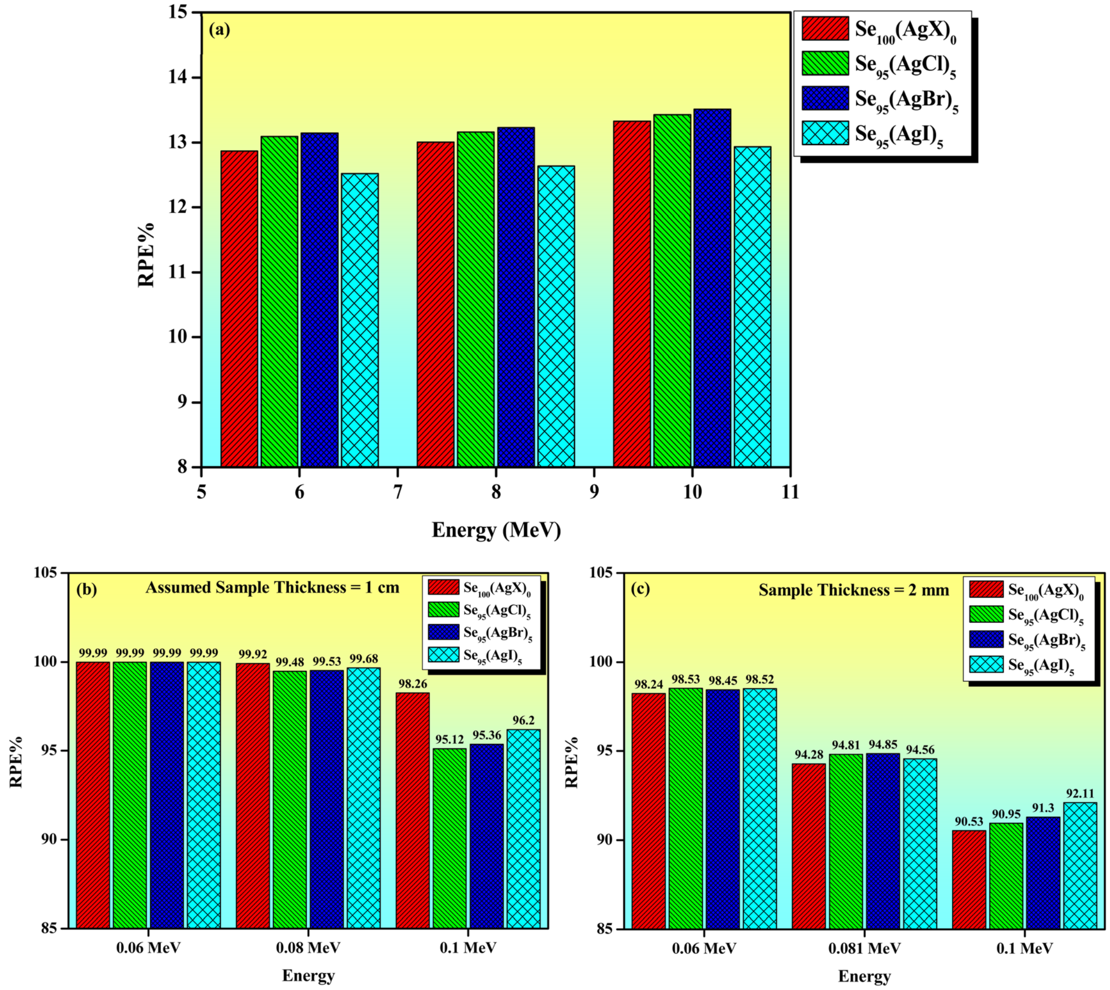

Fig. 15 (a) Theoretical radiation protection effectiveness (RPE%) at photon energies of 6 MeV, 8 MeV, and 10 MeV for all samples, (b) theoretical RPE% and (c) experimental RPE% at 0.06 MeV, 0.08 MeV, and 0.1 MeV photon energies for all samples.

prepared samples at three photon energies: 6 MeV, 8 MeV, and 10 MeV. Fig. 15(b) compares the theoretical RPE% with the experimental RPE% [Fig. 15(c)] for all the same samples at photon energies of 0.06 MeV, 0.08 MeV, and 0.1 MeV, as measured using tungsten source X-ray system in with a Stereotactic field diode detector. Due to experimental limitations, measurements were restricted to these three energies. While the theoretical results suggest higher RPE values, the experimental results are more effective and representative of real-world performance. This discrepancy arises from the difference in sample thickness: theoretical calculations assumed a thickness of 1 cm, whereas the experimental measurements are conducted using 2 mm-thick pellets. Fig. 16 compares the RPE% of the prepared samples with those of commercially used materials and glasses at 0.3 MeV. These bar diagrams show that the sample with silver bromide incorporation displays the maximum RPE%, whereas the sample with silver iodide incorporation exhibits the minimum RPE% among all the compositions. Fig. 16 showed that the Se + AgX samples exhibited the highest radiation protection efficacy among the other materials used for radiation shielding purposes like OC (Ordinary

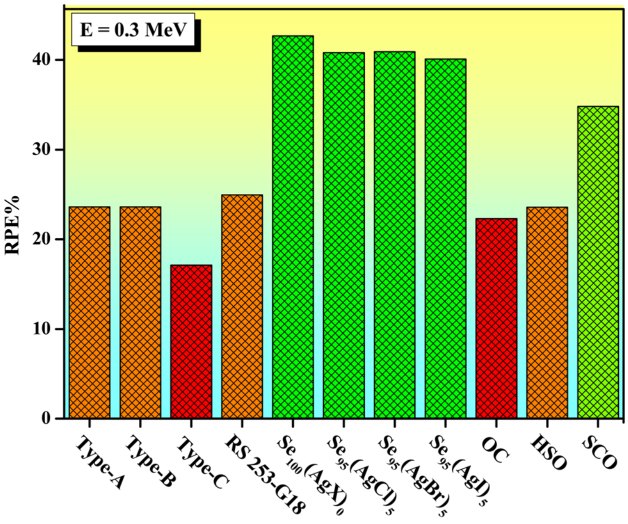

Fig. 16 RPE% comparison of current samples with other materials at 0.3 MeV photon energy.

Table 2 The MAC values for the current glasses and other standard commonly used glasses in radiation shielding applications

		MAC (MeV)		
Samples		0.02	10	
$Se_{100}(AgX)_0$		27.259	0.0342	Reference
$Se_{95}(AgCl)_5$		45.353	0.0321	Present work
$Se_{95}(AgBr)_5$		46.488	0.0323	
$Se_{95}(AgI)_5$		44.664	0.0328	
BPLM 5		11.57	0.023	61
$66B_2O_3$–$5Al_2O_3$–$29Na_2O$		1.074	0.020	
$5Bi_2O_3$–$61B_2O_3$–$5Al_2O_3$–$29Na_2O$		5.059	0.022	
$10Bi_2O_3$–$56B_2O_3$–$5Al_2O_3$–$29Na_2O$		9.043	0.023	
$0PbO$–$30SiO_2$–$46.67B_2O_3$–$23.33Na_2O$		1.386	0.023	62
$5PbO$–$25SiO_2$–$46.67B_2O_3$–$23.33Na_2O$		5.167	0.021	
$10PbO$–$20SiO$–$46.67B_2O_3$–$23.33Na_2O$		8.952	0.024	
$49.46SiO_2$–$26.38Na_2O$–$23.08CaO$–$1.07P_2O_5$		3.982	0.024	63
$47.84SiO_2$–$26.67Na_2O$–$23.33CaO$–$2.16P_2O_5$		3.985	0.023	
$44.47SiO_2$–$27.26Na_2O$–$23.85CaO$–$4.42P_2O_5$		4.057	0.024	
$40.96SiO_2$–$27.87Na_2O$–$24.39CaO$–$6.78P_2O_5$		4.113	0.024	
$37.28SiO_2$–$28.52Na_2O$–$24.95CaO$–$9.25P_2O_5$		4.061	0.024	
30 $Na_2B_4O_7$–70CdO		10.529	0.030	64
$48.98SiO_2$–$26.67Na_2O$–$23.33CaO$–$1.02P_2O_5$		3.983	0.023	
$43.66SiO_2$–$28.12Na_2O$–$24.60CaO$–$3.62P_2O_5$		4.1	0.024	
$38.14SiO_2$–$29.62Na_2O$–$25.91CaO$–$6.33P_2O_5$		4.19	0.022	
$40.71SiO_2$–$28.91Na_2O$–$25.31CaO$–$5.07P_2O_5$		4.131	0.022	
$75SiO_2$–$15Na_2O$–10CaO		3.081	0.0212	65
$74SiO_2$–$15Na_2O$–10CaO–ZrO_2		4.118	0.0215	
$72SiO_2$–$15Na_2O$–10CaO–$3ZrO_2$		6.128	0.0219	
$70SiO_2$–$15Na_2O$–10CaO–$5ZrO_2$		8.058	0.0224	
$68SiO_2$–$15Na_2O$–10CaO–$7ZrO_2$		9.912	0.0229	
$0.5GeS_2$-$0.5Sb_2S_3$	(3.67 g cc^{-3})	20.82	0.034	66
10CsCl–90($0.5GeS_2$–$0.5Sb_2S_3$)	(3.56 g cc^{-3})	20.546	0.034	
20CsCl–80($0.5GeS_2$–$0.5Sb_2S_3$)	(3.42 g cc^{-3})	20.826	0.034	
30CsCl–70($0.5GeS_2$–$0.5Sb_2S_3$)	(3.35 g cc^{-3})	21.124	0.034	
40CsCl–60($0.5GeS_2$–$0.5Sb_2S_3$)	(3.23 g cc^{-3})	21.443	0.035	
$Ge_{20}Sb_6Te_{72}Bi_2$	(6.182 g cc^{-3})	0.34527	0.03819	67
$Ge_{20}Sb_6Te_{70}Bi_4$	(6.229 g cc^{-3})	0.70018	0.03860	
$Ge_{20}Sb_6Te_{68}Bi_6$	(6.299 g cc^{-3})	0.74895	0.03900	
$Ge_{20}Sb_6Te_{66}Bi_8$	(6.384 g cc^{-3})	0.79428	0.03939	
$Ge_{20}Sb_6Te_{64}Bi_{10}$	(6.497 g cc^{-3})	0.84264	0.03972	

Concrete), hematite-serpentine concrete (HSO), steel-scrap concrete (SCO),[60] and some other commercially used glasses; thus, the glass-ceramics studied demonstrated exceptional properties for radiation protection applications. A comparison between the prepared glass ceramics with different glass systems is presented in Table 2.[61–67] It indicated that the Se + AgX had higher MAC values than most other glassy systems; therefore, the glass under investigation had superior characteristics for radiation protection applications.

4. Conclusions

In the presented investigation, we have determined the radiation-shielding characteristic of the pseudo-binary glassy chalco-halide series by implementing open-source code (*Phy-X/PSD*) software. The decreasing sequence of the value of MAC and LAC of the investigated series is like $Se_{95}(AgBr)_5$ > Se95(AgCl)$_5$ > $Se_{95}(AgI)_5$ > $Se_{100}(AgX)_0$. The findings showed that the HVL and MFP values of the glass samples diminished in the sequence: $Se_{95}(AgI)_5$ > $Se_{100}(AgX)_0$ > $Se_{95}(AgCl)_5$ > $Se_{95}(AgCl)_5$. The maximum value of FNRCS is observed for the $Se_{95}(AgCl)_5$ composition. The higher value of MAC and LAC and lower value of HVL and MFP for the $Se_{95}(AgBr)_5$ sample indicate a better composition to attenuate the X-rays and gamma radiation. Therefore, the $Se_{95}(AgBr)_5$ glassy sample is an excellent choice for gamma shielding applications across various sectors. The experimental attenuation data for the 2 mm thick sample further confirms the potential of these pseudo-binary glass ceramics for radiation shielding applications. However, to attenuate the fast neutrons, $Se_{95}(AgCl)_5$ composition is better among all studied glassy compositions. Furthermore, the comparison proves that these chalcogenide materials exhibit superior radiation-shielding capability than other commercial materials and glasses.

Nevertheless, the study is subject to certain limitations. The experimental dataset was constrained by the limited availability of sample material, restricting the breadth of energy levels tested. Furthermore, due to the unavailability of high-energy gamma-ray experimental setups, validation at energies beyond 1.5 MeV relied solely on computational predictions. These factors highlight the need for broader experimental access and material scalability in future investigations. Future work will focus on scaling up sample production to enable more extensive experimental validation, particularly in high-energy photon environments. Additionally, we plan to explore compositional tuning and the fabrication of multilayered or hybrid shielding architectures to optimize performance across a broader energy spectrum. Integration with flexible or transparent matrices may also be explored to extend applicability in wearable and structural shielding systems.

Data availability

All data supporting this article are included in the main manuscript as figures and tables.

Author contributions

Anil Kumar, Shiv Kumar Pal, and N. Mehta: plotting graphs, writing – original draft, and conceptualization.

Conflicts of interest

The authors declare that they have no known competing financial interests or personal relationships that could have appeared to influence the work reported in this paper.

Acknowledgements

We gratefully acknowledge Prof. S. D. Sharma and Mr Rahul Kumar Chaudhary from the Medical Physics Section, BARC, Mumbai, as well as the Central Discovery Centre of our university, for providing the necessary instrumental facilities. Anil Kumar is grateful to the UGC, New Delhi, India, for providing the fellowship under the Joint CSIR-UGC JRF scheme (Award Ref. No. 231610089401). Prof. Neeraj Mehta is thankful to his university for providing an incentive grant under the Institutes of Eminence (IoE) scheme (Dev. Scheme No. 6031-B).

References

1 M. Elsafi, M. Sayyed, T. A. Hanafy, C. V. More and A. Hedaya, Experimental study of gamma-ray attenuation capability of B_2O_3–ZnO–Na_2O–Fe_2O_3 glass system, *Sci. Rep.*, 2024, **14**, 19141.

2 S. Yasmin, B. Barua, M. U. Khandaker, F. Chowdhury, M. Rashid, D. Bradley, M. A. Olatunji and M. Kamal, Studies of ionizing radiation shielding effectiveness of silica-based commercial glasses used in Bangladeshi dwellings, *Res. Phys.*, 2018, **9**, 541–549.

3 M. A. Imheidat, M. KhHamad, K. A. Naseer, M. Sayyed, N. Dwaikat, K. Cornish, Y. Alajerami, M. Alqahtani and M. Mhareb, Radiation shielding, mechanical, optical, and structural properties for tellurite glass samples, *Optik*, 2022, **268**, 169774.

4 A. Saeed, R. M. El Shazly, Y. H. Elbashar, A. M. Abou El-Azm, M. N. H. Comsan, M. M. El-Okr and W. A. Kansouh, Glass materials in nuclear technology for gamma-ray and neutron radiation shielding: a review, *Nonlinear Opt, Quantum Opt.*, 2021, **53**, 107–159.

5 I. Kebaili, I. Boukhris, Z. A. Alrowaili, M. M. Abutalib and M. S. Al-Buriahi, Characterization of physicochemical properties of As_2Se_3–GeTe–AgI chalcohalide glasses for solar cell and IR applications: influence of adding AgI, *J. Mater. Sci.: Mater. Electron.*, 2022, **33**, 800–809.

6 D. D. Salimgareev, A. A. Lashova, A. S. Shmygalev, E. A. Korsakova, B. P. Zhilkin, A. S. Korsakov and L. V. Zhukova, Influence of geometrical parameters on transmitting thermal radiation through silver halide fibers, *Results Phys.*, 2020, **16**, 102994.

7 S. Ding, Z. Liu, S. Dai, C. Liu and Z. Cao, Novel acousto-optic material based on Ge-Te-AgI chalcohalide glasses, *Ceram. Inter.*, 2021, **47**, 12072–12077.

8 R. Patwari and B. Eraiah, Investigation of gamma radiation effect on bismuth borate glasses doped with europium oxide and silver chloride, *Indian J. Pure Appl. Phys.*, 2018, **56**, 600–603.

9 H. E. Atyia, S. S. Fouad, S. K. Pal, A. Srivastava and N. Mehta, Study of optical bandgap and other related optical properties in amorphous thin films of some optical materials of .Se-Te-Sn-Ag system, *Indian J. Pure Appl. Phys*, 2022, **150**, 107985.

10 W. Shen, S. Baccaro, A. Cemmi, J. Ren, Z. Zhang, Y. Zhou, Y. Yang and G. Chen, Gamma-ray irradiation resistance of silver doped GeS_2–Ga_2S_3–AgI chalcohalide glasses, *NIM-B*, 2014, **329**, 48–51.

11 C. B. Childs and T. A. Parnell, Heavy ion passive dosimetry with silver halide single crystals, *Proc. Nat. Symp. Nat. Manmade Rad. Space*, 1972, 138–141.

12 M. J. Danielson, Effect of Gamma Radiation on Stability of Silver-Silver Chloride and Mercury-Calomel Commercial Reference Electrodes, *Corrosion*, 1995, **51**, 450–455.

13 N. A. Kawady, M. Elkattan, M. Salah and A. A. Galhoum, Fabrication, characterization, and gamma-ray shielding properties of PVA-based polymer nanocomposite, *J. Mater. Sci.*, 2022, **57**, 11046–11061.

14 S. Ud-Din Khan, S. Ud-Din Khan, Z. Almutairi, S. Haider and S. M. Ali, Development of theoretical-computational model for radiation shielding, *J. Rad. Res. Appl. Sci.*, 2020, **13**, 606–615.

15 R. A. Elsad, K. A. Mahmoud, Y. S. Rammah and A. S. Abouhaswa, Fabrication, structural, optical, and dielectric properties of PVC-PbO nanocomposites, as well as their gamma-ray shielding capability, *Rad. Phys. Chem.*, 2021, **189**, 109753.

16 C. Zeng, Q. Kang, Z. Duan, B. Qin, X. Feng, H. Lu and Y. Lin, Development of Polymer Composites in Radiation Shielding Applications: A Review, *J. Inorg. Organometal. Poly. Mater.*, 2023, **33**, 2191–2239.

17 M. Shahzad, S. Shahid, Z. A. Rehan, T. Zhao, K. Fatima, H. M. F. Shakir and I. Shahid, Enhanced electromagnetic interference shielding using Nanosilver-Decorated

Graphene/Poly(vinyl chloride) nanocomposite films, *Mate. Chem. Phys.*, 2024, **314**, 128817.

18 A. A. Al-Ghamdi and F. El-Tantawy, New electromagnetic wave shielding effectiveness at microwave frequency of polyvinyl chloride reinforced graphite/copper nanoparticles, *Composites, Part A*, 2010, **41**, 1693–1701.

19 A. A. Al-Ghamdi, F. El-Tantawy, N. A. Aal, E. H. El-Mossalamy and W. E. Mahmoud, Stability of new electrostatic discharge protection and electromagnetic wave shielding effectiveness from poly(vinyl chloride)/graphite/nickel nano conducting composites, *Polym. Degrad. Stab.*, 2009, **94**, 980–986.

20 Z. Yang, L. Luo and W. Chen, Red Color $GeSe_2$-Based Chalcohalide Glasses for Infrared Optics, *J. Am. Ceram. Soc.*, 2006, **89**, 2327–2329.

21 D. Mihailovic, Inorganic molecular wires: Physical and functional properties of transition metal chalco-halide polymers, *Prog. Mater. Sci.*, 2009, **54**, 309–350.

22 M. Nowak, M. Jesionek and K. Mistewicz, *Applications of Group 15 Ternary Chalcohalide Nanomaterials*, Ind. Appl. Nanomater., 2019, pp. 225–282.

23 I. Kebaili, I. Boukhris and A. Dahshan, Investigation of the correlation between physicochemical, optical and thermal properties of $(GeS_2)_{60}(Sb_2S_3)_{40-x}(CdCl_2)_x$ chalcohalide glasses, *Phys. Scr.*, 2020, **95**, 085704.

24 L. Yunmeng, P. Jincong, Z. Qingli, H. Song, X. Ling, L. Wei, Z. Zheng and G. Niu, BiSBr, an Anisotropic One-Dimensional Chalcohalide Used for Radiographic Detection, *J. Phys. Chem. C*, 2024, **128**, 3839–3843.

25 S. Johnsen, Z. Liu, J. A. Peters, J.-H. Song, S. Nguyen, C. D. Malliakas, H. Jin, A. J. Freeman, B. W. Wessels and M. G. Kanatzidis, Thallium Chalcohalides for X-ray and γ-ray Detection, *J. Am. Chem. Soc.*, 2011, **133**, 10030–11003.

26 M. Zhang, Z. Yang, H. Zhao, A. Yang, L. Li and H. Tao, Glass forming and properties of Ga_2S_3–Sb_2S_3–CsCl chalcohalide system, *J. Alloys Compds.*, 2017, **722**, 166–172.

27 Z. Feng, J. Wang, G. Wu, J. Wang, T. Huang, W. Sun, Y. Wang, J. Sheng, Q. Peng, K. Yang, Z. Zhao, S. Bai, X. Wang, R. Wang, S. Dai and Q. Nie, Research on a novel chalcohalide glass and its physical optics properties, *Infrared Phys. Technol.*, 2022, **122**, 104079.

28 A. E. Ersundu, M. I. Sayyed, O. Kıbrıslı, V. Akıllı and M. C. Ersundu, A thorough investigation of the Bi_2O_3–$PbCl_2$–TeO_2 system: glass forming region, thermal, physical, optical, structural, mechanical and radiation shielding properties, *J. Alloys Compd.*, 2021, **857**, 158279.

29 M. I. Sayyed, M. C. Ersundu, A. E. Ersundu, G. Lakshminarayana and P. Kostka, Investigation of radiation shielding properties for MeO–$PbCl_2$–TeO_2 (MeO = Bi_2O_3, MoO_3, Sb_2O_3, WO_3, ZnO) glasses, *Rad. Phys. Chem.*, 2018, **144**, 419–425.

30 V. Saraswat, A. Dahshan, H. I. Elsaeedy, Z. Khattari and N. Mehta, High-energy radiation shielding characteristics of SeTeSnAg chalcogenide glasses (STSA ChGs), *Opt. Mater.*, 2024, **148**, 114886.

31 S. K. Pal, A. Kumar and N. Mehta, Signature of rigidity percolation effect in dielectric behavior of germanium containing multi-component chalcogenide glasses (ChGs), *Ceram. Inter.*, 2019, **45**, 16279–16287.

32 A. Kumar, V. Saraswat, A. Dahshan, H. I. Elsaeedy and N. Mehta, Exploring dielectric and AC conduction characteristics in elemental selenium glass modified with silver halides, *RSC Adv.*, 2024, **14**, 20933.

33 S. K. Yadav, A. Dahshan and N. Mehta, Tuning dielectric, mechanical, and electrical properties in rGO/graphite-reinforced selenium nanocomposites, *Ceram. Inter.*, 2025, 0272–8842.

34 G. W. Tang, Q. Qian, K. L. Peng, X. Wen, G. X. Zhou, M. Sun and Z. M. Yang, Selenium semiconductor core optical fibers, *AIP Adv.*, 2015, **5**, 027113.

35 P. Cherin and P. Unger, The crystal structure of trigonal selenium, *Inorg. Chem.*, 1967, **6**, 1589–1591.

36 S. Hull and D. A. Keen, Pressure-induced phase transitions in AgCl, AgBr, and AgI, *Phys. Rev. B: Condens. Matter Mater. Phys.*, 1999, **59**, 750–761.

37 A. H. Goldan, C. Li, S. J. Pennycook, J. Schneider, A. Blom and W. Zhao, Molecular structure of vapor-deposited amorphous selenium, *J. Appl. Phys.*, 2016, **120**, 135101.

38 M. Marple, J. Badger, I. Hung, Z. Gan, K. Kovnir and S. Sen, Structure of Amorphous Selenium by 2D ^{77}Se NMR Spectroscopy: An End to the Dilemma of Chain *versus* Ring, *Angew. Chem., Int. Ed.*, 2017, **56**, 9777–9781.

39 S. K. Yadav, A. Kumar and N. Mehta, Synthesis and characterization of nanostructured graphene-doped selenium, *RSC Adv.*, 2023, **13**, 13564.

40 G. Bottger and C. Damsgard, Second order Raman spectra of AgCl and AgBr crystals, *Solid State Commun.*, 1971, **9**, 1277–1280.

41 T. S. V. Nguyen, T. M. Huynh, T. D. To, T. C. Doan and C. M. Dang, Ag/AgCl film electrodes coated with agarose gel as planar reference electrodes for potentiometric sensors, *Univers. J. Mater. Sci.*, 2018, **6**, 148–154.

42 G. Burns, F. H. Dacol and M. W. Shafer, Results from Raman spectra of the superionic conductor AgI, *Phys. Rev. B: Condens. Matter Mater. Phys.*, 1977, **16**, 1416.

43 E. Şakar, Ö. F. Özpolat, B. Alım, M. I. Sayyed and M. Kurudirek, *Phy-X/PSD*: development of a user-friendly online software for calculation of parameters relevant to radiation shielding and dosimetry, *Rad. Phys. Chem.*, 2020, **166**, 108496.

44 A. Kumar and N. Mehta, Correlation between some thermo-mechanical and physico-chemical properties in multi-component glasses of Se–Te–Sn–Cd system, *Appl. Phys. A*, 2017, **123**, 410.

45 K. A. Mahmoud, M. I. Sayyed and O. L. Tashlykov, Gamma-ray shielding characteristics and exposure buildup factor for some natural rocks using MCNP-5 code, *Nucl. Engin. Technol.*, 2019, **51**, 1835–1841.

46 K. Saraswat, S. K. Pal, Z. Y. Khattari, A. Dahshan and N. Mehta, A comprehensive study of radiation shielding parameters of chalcogens-rich quaternary alloys for nuclear waste management, *Opt. Mater.*, 2024, **157**, 116253.

47 M. Hanfi, A. Sakr, A. M. Ismail, B. M. Atia, M. Alqahtani and K. Mahmoud, Physical characterization and radiation

shielding features of $B_2O_3As_2O_3$ glass ceramic, *Nucl. Eng. Technol.*, 2023, **55**, 278–284.

48 O. Olarinoye, Variation of effective atomic numbers of some thermoluminescence and phantom materials with photon energies, *Res. J. Chem. Sci.*, 2011, **1**, 64–69.

49 S. Gowda, S. Krishnaveni and R. Gowda, *Studies on Effective Atomic Numbers and Electron Densities in Amino Acids and Sugars in the Energy Range 30–1333 keV*, NIM-B, 2005, vol. 239, pp. 361–369.

50 A. H. El-Kateb, R. A. M. Rizk and A. M. Abdul-Kader, Determination of Atomic Cross-Sections and Effective Atomic Numbers for Some Alloys, *Ann. Nucl. Energy*, 2000, **27**, 1333–1343.

51 G. Kilic, E. Ilik, S. A. M. Issa, B. Issa, U. G. Issever, H. M. H. Zakaly and H. O. Tekin, Fabrication, structural, optical, physical and radiation shielding characterization of indium (III) oxide reinforced $85TeO_2$–$(15–x)ZnO$–xIn_2O_3 glass system, *Ceram. Inter.*, 2021, **47**, 27305–27315.

52 Y. Harima, Y. Sakamoto, S. Tanaka and M. Kawai, Validity of the geometric progression formula in approximation of gamma ray buildup factors, *Nucl. Sci. Eng.*, 1986, **94**, 24–28.

53 M. I. Sayyed and H. Elhouichet, Variation of energy absorption and exposure buildup factors with incident photon energy and penetration depth for boro-tellurite (B_2O_3–TeO_2) glasses, *Rad. Phys. Chem.*, 2017, **130**, 335–342.

54 A. M. Adefisoye, S. Idowu and A. Sado, Investigation of the Effects of Buildup Factors on Electromagnetic Radiation Dose, *J. Eng. Exact Sci.*, 2024, **10**, 18837.

55 I. Boukhris, M. S. Al-Buriahi, H. Akyildirim, A. Alalawi, I. Kebaili and M. I. Sayyed, Chalcogenide glass-ceramics for radiation shielding applications, *Ceram. Inter.*, 2020, **46**, 19385–19392.

56 B. Alıma, E. Şakar, İ. Han and M. I. Sayyed, Evaluation the gamma, charged particle and fast neutron shielding performances of some important AISI-coded stainless steels: Part II, *Rad. Phys. Chem.*, 2020, **166**, 108454.

57 B. Tellili, Y. Elmahroug and C. Souga, Calculation of fast neutron removal cross sections for different lunar soils, *Adv. Space Res.*, 2014, **53**, 348–352.

58 V. Saraswat, Z. Y. Khattari and N. Mehta, Analysis of high-energy radiation shielding features of SeTeSn glass after incorporation of bismuth, *Mater. Today Commun.*, 2024, **39**, 108995.

59 V. Saraswat, A. Dahshan, Z. Khattari and N. Mehta, High-energy radiation shielding characteristics of SeTeSnZn chalcogenide glasses (STSZ ChGs), *Prog. Nucl. Energy*, 2024, **173**, 105224.

60 G. Almisned, H. Zakaly, S. Issa, A. Ene, G. Kilic, O. Bawazeer, A. Almatar, D. Shamsi, El Rabaa, Z. Sideig and H. Tekin, Gamma-ray protection properties of bismuth-silicate glasses against some diagnostic nuclear medicine radioisotopes: a comprehensive study, *Materials*, 2021, **14**, 6668.

61 K. S. Shaaban, H. Y. Zahran, I. S. Yahia, H. I. Elsaeedy, E. R. Shaaban, S. A. Makhlouf, E. Wahab and E. S. Yousef, Mechanical and radiation-shielding properties of B_2O_3–P_2O_5–Li_2O–MoO_3 glasses, *Appl. Phys. A*, 2020, **126**, 1–11.

62 S. Issa, Y. Saddeek, H. O. Tekin, M. Sayyed and K. Shaaban, Investigations of radiation shielding using Monte Carlo method and elastic properties of PbO-SiO_2-B_2O_3-Na_2O glasses, *Curr. Appl. Phys.*, 2018, **18**, 717–727.

63 K. Mahmoud, A. Alsubaie, E. Wahab, F. Abdel-Rahim and K. Shaaban, Research on the Effects of Yttrium on Bismuth Titanate Borosilicate Glass System, *Silicon*, 2022, 1–9.

64 A. El-Rehim, H. Zahran, I. S. Yahia, S. Makhlouf and K. Shaaban, Radiation, crystallization, and physical properties of cadmium borate glasses, *Silicon*, 2021, **13**, 2289–2307.

65 H. Akyildirim, E. Kavaz, F. I. El-Agawany, E. Yousef and Y. Rammah, Radiation shielding features of zirconolite silicate glasses using XCOM and FLUKA simulation code, *J. Non-Cryst. Solids*, 2020, **545**, 120245.

66 I. Boukhris, M. S. Al-Buriahi, H. Akyildirim, A. Alalawi, I. Kebaili and M. I. Sayyed, Chalcogenide glass-ceramics for radiation shielding applications, *Ceram. Inter.*, 2020, **46**, 19385–19392.

67 J. S. Alzahrani, Z. A. Alrowaili, C. Mutuwong, I. O. Olarinoye and M. S. Al-Buriahi, Radiation shielding competence of chalcogenide alloys with high Te content, *Appl. Radiat. Isot.*, 2023, **196**, 110759.